Rock Mechanics and Rock Engineering
https://doi.org/10.1007/s00603-019-02032-y

ORIGINAL PAPER

Experimental Investigation of the Effect of Salt Precipitation on the Physical and Mechanical Properties of a Tight Sandstone

Dujie Zhang[1,2] · Yili Kang[1] · A. P. S. Selvadurai[2] · Lijun You[1]

Received: 30 April 2019 / Accepted: 10 December 2019

Abstract
Salt precipitation in rocks is a strongly coupled physico-chemical process, which has implications on natural gas extraction efficiency. The paper examines the effect of salt precipitation on porosity, permeability, permeability-stress sensitivity and elastic wave velocities of the rock matrix in tight sandstone with high salinity. Results show that the porosity and permeability decrease significantly after salt precipitation, and the permeability-stress sensitivity was aggravated by the salt precipitation. Following salt precipitation, the elastic wave velocities decreased significantly, the dynamic Young's modulus of the rock decreased, and the dynamic Poisson's ratio increased. Microstructural analysis suggests that following salt precipitation, the smaller pores and pore throats become the main seepage channels. The crystalline salt was deposited in the pores, the micro-fractures and on the surface of clay minerals, which not only reduces porosity and permeability, but contributes to the development of secondary cracks that weaken the rock matrix.

Keywords Tight sandstone · Salt precipitation · Permeability-stress sensitivity · Elastic wave velocities · Secondary cracks

1 Introduction

Salt precipitation is a common phenomenon encountered in many engineering endeavours, including the control of water loss from land surfaces (Scanlon et al. 1997), protection of pavements, roads and historical monuments (Flatt 2002; Espinosa-Marzal and Scherer 2010), and various geochemical issues related to intact geological formations (Shahidzadeh-Bonn et al. 2010). The mechanism for salt precipitation in deep geological formations is more complex than those encountered on surficial soils. For example, CO_2 sequestration (Rathnaweera et al. 2015; Zhou et al. 2016), enhanced geothermal systems (Borgia et al. 2012; Cui et al. 2018), and natural gas production (Cui et al. 2016) are all situations, where salt precipitation can influence injectivity and productivity if salt precipitation causes alterations to the porosity and permeability of the geologic medium.

✉ Dujie Zhang
dujie.zhang@qq.com; dujie.zhang@mail.mcgill.ca

1 State Key Laboratory of Oil and Gas Reservoir Geology and Exploitation, Southwest Petroleum University, Chengdu 610500, Sichuan, People's Republic of China

2 Department of Civil Engineering and Applied Mechanics, McGill University, Montréal, QC H3A OC3, Canada

Field observations of salt deposition in gas wells indicated that salt crystals can gather in the wellbore and perforation zone, which affects the reservoir yield during gas production (Kleinitz et al. 2001). With reference to natural gas extraction, the gas reservoir can be divided into three zones depending on the degree of water evaporation: the *Precipitation Zone*, the *Water Movement Zone* and the *In-situ Zone,* as shown in Fig. 1. In the *Precipitation Zone*, the pressure declines around the wellbore causing an increase in the molar water content of the flow space, which leads to evaporation of water. When the solubility of the dissolved ions exceeds the critical solubility, salt deposition occurs (Van Dorp et al. 2009). In the *Water Movement Zone*, the irreducible formation water and the invasive filtrate of the water-based working fluids move to the *Precipitation Zone* due to the high osmotic potential and residual capillary forces (Miri and Hellevang 2016). This zone changes with the development of the gas reservoir. In the *In-situ Zone*, the gas reservoir is in its original state, and there is no salt precipitation or formation water movement.

The *Precipitation Zone* is the area that is most affected by salt precipitation. In this zone, salt precipitation has been considered as the cause of permeability reduction in some gas fields and as a potential problem in many others (Kirk and Dobbs 2002; Kim et al. 2012). Work has been conducted

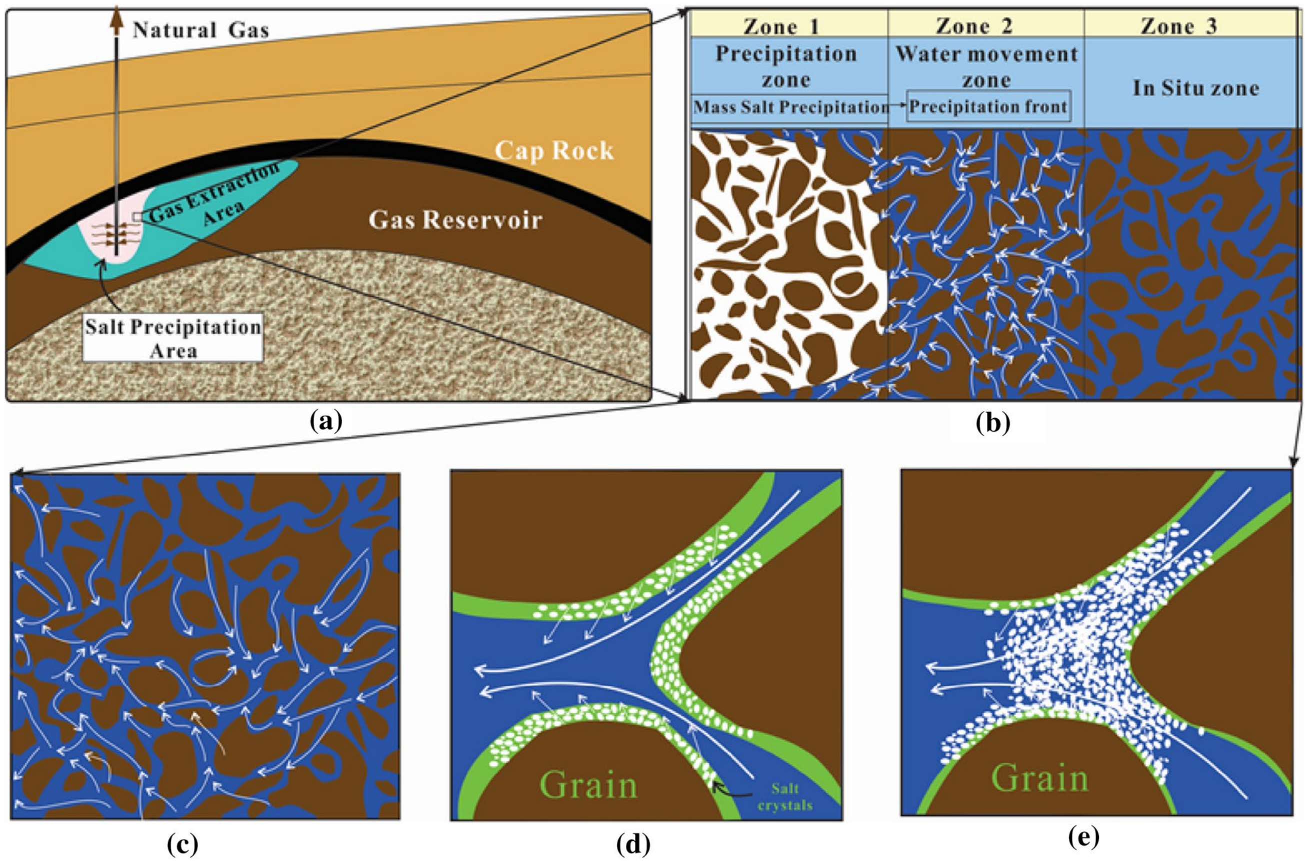

Fig. 1 Schematic diagram of salt precipitation during gas production in tight sandstone gas reservoirs. **a** The view of the damaged regions induced by salt precipitation at the gas reservoir scale, **b** the division of the Precipitation Zone, the Water Movement Zone and the In-situ Zone, **c** the transport of the high salinity formation water during gas production, **d** salt crystallizes and precipitates once the salinity of formation water exceeds the critical concentration, **e** crystalline salt moves and gathers in the seepage channels

on the kinetics and the influencing parameters of salt precipitation to clarify the mechanism of salt precipitation in hydrocarbon-bearing porous rocks. Espinosa-Marzal and Scherer (2013) and Tang et al. (2015) showed that the pore clogging induced by salt precipitation is affected by the type of salt (NaCl, KCl, Na_2SO_4 and $MgSO_4$) and the pore structure of the host rock. Ott et al. (2014) observed the capillary-driven transport of formation water and the respective solutes at the pore scale. They observed that the transport of solute between porosity classes determines the distribution of the deposited salt in the pore space and the relationship between permeability and porosity for flow-through drying. Le and Mahadevan (2011) developed a model for evaporation in productive gas wells, including the effect of capillary pressure, and suggested that the higher the capillary pressure, the more salt is crystallized and precipitated, resulting in a larger permeability reduction for the gas well. When salt minerals are precipitated in confined pores, the induced crystallization stress can potentially damage the gas reservoir (Winkler and Singer 1972; Rijniers et al. 2005). Noiriel et al. (2010) investigated the effects of sodium chloride precipitation induced by water evaporation on fractures in sandstone; their results showed that fracture networks were formed by nucleation of micro-fractures in the region, where water evaporation occurred. The extent and degree of salt damage in porous rocks caused by crystallization pressure could be a function of many processes and parameters including the crystal liquid interfacial free energy, the solution super saturation, the growth rate of crystals, the localization of precipitation and the mechanical response of the host rock and its in situ stress state (Noiriel et al. 2010; Flatt et al. 2014; Zheng et al. 2015). The change in the rock mesostructure due to salt precipitation alters the mechanical properties of the reservoir rock; this is reflected in the gas well production, because it influences the stress-sensitivity permeability of the gas reservoir.

Recently, high-pressure/high-temperature and high yield tight sandstone gas reservoirs containing high-salinity brine have been developed and the corresponding problem of salt precipitation has become more evident. Investigations to assess the influence of salt precipitation on the properties of a tight sandstone gas reservoirs are, however, scarce.

The ultra-deep (> 7000 m) tight sandstone gas reservoirs with high salinity brine located in the Tarim Basin, were investigated to determine the effect of salt precipitation on the physical and mechanical properties of a tight sandstone with high salinity formation water. First, the porosity and permeability of the matrix before and after salt precipitation were investigated in a laboratory setting. Then, the permeability-stress sensitivity and the elastic wave velocities of the rock were measured. In addition, high-pressure mercury injection tests and Scanning Electron Microscopy were used to analyze the microstructural changes that followed salt precipitation.

2 Materials and Methods

2.1 Materials

Fourteen tight sandstone core samples (2.54 cm in diameter and 3.00–6.00 cm in length) were recovered from typical ultra-deep tight sandstone gas reservoirs in the K gas field, Tarim Basin, China. The porosity of the samples ranged from 1 to 5%, and the gas permeability was $0.01 \sim 0.035 \times 10^{-3}$ μm^2. The basic physical properties of the samples that were tested are as shown in Table 1. The salinity of the in situ brine in the tight gas reservoirs was approximately 200,000 mg/L ~ 210,000 mg/L. To ensure the consistency of the experiments, the brine solution used in this research was prepared in the laboratory according to the ion constitution of the formation water obtained from the K gas reservoirs. The composition of the brine solution is $NaHCO_3$ (243.6 mg/L), Na_2SO_4 (604.9 mg/L), NaCl (171,497.0 mg/L), $MgCl_2$ (3744.0 mg/L) and $CaCl_2$ (28,837.8 mg/L) (Zhang et al. 2018).

2.2 Water Saturation and Salt Precipitation

As mentioned in the Induction, the water saturation of the in situ samples is variable. If the oil and gas reservoir contains bottom water or product formation water from oil and gas production, the in situ water saturation of the formation could reach up to 100%. Therefore, the samples were prepared with water saturations of 10%, 20%, 40%, 60% and 100%. The accuracy of the targeted saturations is 0.1%. A spontaneous capillary water imbibition experiment (Dehghanpour et al. 2013) was performed to establish the initial water saturation of the samples with 10%, 20%, 40% and 60% water saturation. For fully saturated samples, fluid was evacuated with a vacuum pump for 12 h in an autoclave body, and brine was allowed to fill the autoclave body. The liquid pressure was then increased to 20 MPa for 24 h to make sure that the sample was completely saturated with brine. Salt precipitation experiments were then conducted. In salt precipitation experiments, it is necessary for evaporation to occur on the rock surface during salt precipitation, i.e., the samples were allowed to dry from all sides. Therefore, it is not possible to consider the in situ stress and real pore pressure values during salt precipitation. If the temperature of the experiment is set as the real value without the real gas pressure, the high temperatures would promote the transformation of the clay minerals; for example, montmorillonite can be transformed into illite and analcime, and kaolinite can be transformed to montmorillonite and analcime due to the water sensitivity of the clay mineral, whereas illite is relatively stable. Such transformations of the clay minerals would cause significant changes in the pore structure (Zhuang et al. 2018), resulting in changes to the porosity and permeability of the sample, which would influence the experimental results of salt precipitation. To

Table 1 The basic physical properties of the experimental samples

Sample no.	Depth (m)	Length (mm)	Diameter (mm)	Porosity (%)	Permeability ($\times 10^{-3}$ μm^2)	Pore volume (ml)
KS1-7	7733.38	51.01	24.78	4.79	0.0155	1.178
KS1-15	7850.46	49.98	24.78	4.04	0.0349	0.973
KS5-4	7755.45	49.58	24.70	3.71	0.0241	0.881
KS5-5	7758.32	23.25	24.50	3.56	0.0229	0.390
KS3-4	7898.96	45.52	24.72	1.69	0.0305	0.369
KS3-9	7907.43	54.38	24.72	1.93	0.0208	0.503
KS4-1	7651.73	53.12	24.78	2.79	0.0127	0.714
KS6-7	7564.73	51.70	24.92	2.13	0.0135	0.537
KS5-12	7792.28	50.90	24.84	2.80	0.0172	0.690
KS5-14	7794.37	31.22	24.50	2.58	0.0182	0.380
KS5-13	7793.57	50.22	24.72	2.66	0.0162	0.641
KS5-15	7795.01	47.63	24.60	2.93	0.0141	0.663
KS1-17	7851.82	47.05	24.25	2.81	0.0128	0.610
KS1-23	7971.77	46.56	24.25	3.40	0.0329	0.731

investigate more accurately the effect of salt precipitation on the physical and mechanical properties of a tight sandstone, salt precipitation experiments was conducted. A schematic of the salt precipitation experiments and use of the sample for microstructural observations is shown in Fig. 2. Detailed experimental procedures of salt precipitation are as follows: (1) the sample with an initial water saturation was placed in air oven; (2) the sample was kept vaporized at 60 °C and at ambient pressure until no further changes in the weight of the sample were observed; and (3) the salt precipitation experiment was completed, and the samples were removed for other experiments.

2.3 Porosity, Permeability and Permeability-stress Sensitivity Measurements

The experimental research focused on the laboratory estimation of porosity, permeability and permeability-stress sensitivity alterations in a cylindrical sandstone sample before and after salt precipitation: (1) Nitrogen was used to determine the porosity of the samples under a

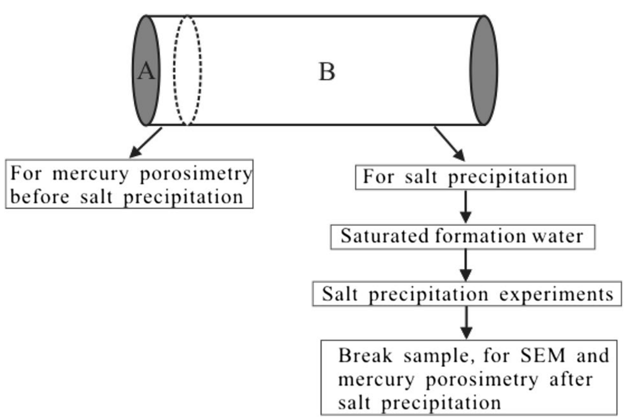

Fig. 2 Schematic of the water saturation experiment, salt precipitation experiments and use of the sample for microstructural observations

constant confining pressure (3 MPa) (according to Boyle's law, $P_1V_1 = P_2V_2$). (2) For the permeability testing, the samples were tested under a fixed confining pressure (3 MPa), an inlet pressure of 1.6 MPa and an outlet pressure of 0.6 MPa to minimize gas slippage effects (Tian et al. 2018). The gas permeability was measured using 99.9% pure dry nitrogen gas supplied at room temperature (25 °C). The gas flow rate was measured using a Sevenstar D07-11CM semi-conductor flow meter (0.005 mL/min). A schematic view of the experimental facility is shown in Fig. 3.

(3) Two untreated tight sandstone samples and two samples after salt precipitation (initial water saturation 100%) were selected for the permeability-stress sensitivity experiments. The experimental procedures for permeability-stress sensitivity testing are similar to those used for permeability testing, but with variable all-round confining pressure. Confining pressures of 3 MPa, 5 MPa, 10 MPa, 15 MPa, 20 MPa, 25 MPa and 30 MPa were applied and removed quasi-statically. The isotropic effective stress σ was obtained based on Biot's effective stress principle (Biot 1941); from rock mechanics experiments, the average Biot coefficient of these matrix samples was set to 0.38 (Selvadurai 2018; Selvadurai et al. 2018), and the corresponding effective stress was calculated using Eq. 1:

$$\sigma = P_c - \alpha P_f, \tag{1}$$

where σ is the effective stress, MPa; P_c is the confining pressure, MPa; P_f is the pore pressure, MPa; α is the Biot coefficient. Xu et al. (2018) assumed that the seepage in the sample was a plate flow, allowing them to define the stress sensitivity coefficient parameter. The physical meaning of the stress sensitivity coefficient is the degree of change in the equivalent seepage channel aperture with an increase in the effective stress. Therefore, in this paper, the stress sensitivity coefficient (S_{si}) is used to evaluate the change in permeability under confining pressure, and is expressed as follows:

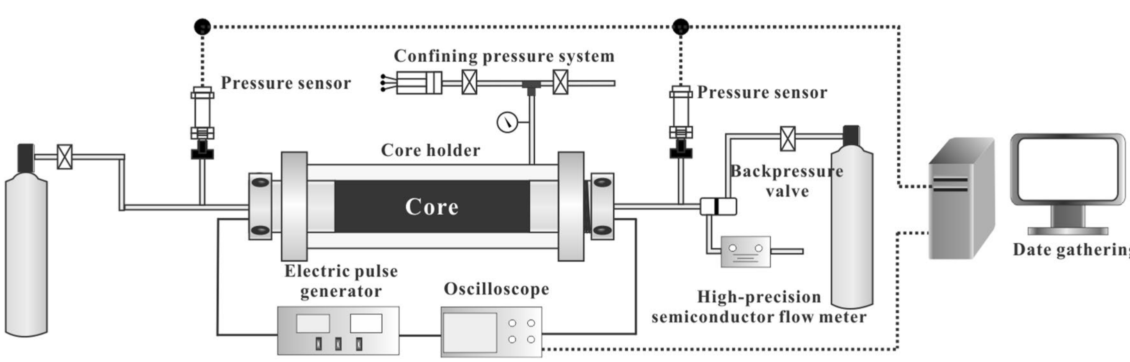

Fig. 3 Schematic view of the experimental facility for measuring permeability, permeability-stress sensitivity and acoustic wave velocity

$$S_{\mathrm{si}} = \frac{1 - \sqrt[3]{K_i/K_0}}{\log_{10}(\sigma_i/\sigma_0)}, \tag{2}$$

where K_0 is the initial permeability, $\times 10^{-3}$ μm^2; K_i is the permeability in the ith test point ($i = 1, 2, 3\ldots$), $\times 10^{-3}$ μm^2; σ_0 is the initial effective stress, MPa; σ_i is the effective stress in the ith test point, MPa.

2.4 Measurement of Elastic Wave Velocities

Elastic wave velocities [Compressional waves (P-waves) and shear waves (S-waves)] were induced by an electric pulse generator. The rise duration of the generator was a maximum of 0.2 ms. The frequency of P-waves and S-waves emitted by the electric pulse generator was 960 kHz and 620 kHz, respectively, with an accuracy of 0.1 μs. This generator was connected to transmitter/receptor transducers. The sample was placed between the transducers in a core holder subjected to 3 MPa of confining pressure. A RIGOL DS1052E oscilloscope (10 ns-time resolution) was used to register the signals. The experimental was performed at room temperature (25 °C).

2.5 Microstructural Observations

Any microstructural variations, the morphology and location of crystalline salt in the rock masses after salt precipitation were identified using a Scanning Electron Microscope (SEM). The SEM (Quanta 250, FEI) was used in a low vacuum mode to capture the changes in the tight sandstone micro-structure, and the test accuracy ranged from 100 nm to 3 500 μm. The pore size distribution of the sample was measured using a high-pressure mercury porosimeter (PoreMaster 60GT, Quantachrome Instruments). The measured pore size ranged from 1.8 nm to 150 μm, and the maximum mercury injection pressure was 400 MPa. It should be emphasized that the salt experiment samples and the mercury porosimetry samples were not the same sample, but were taken from the same core plug. As shown in Fig. 2, the core plug was divided into Part A and Part B. Part A was used to conduct the mercury porosimetry experiment before salt precipitation. Part B was used to conduct the salt precipitation experiment and the follow-up evaluation experiments; the sample length of Part B was close to 50 mm. After the follow-up evaluation experiment was completed, Part B was prepared for the mercury porosimetry experiment after salt precipitation.

3 Results and Discussion

3.1 Porosity and Permeability Changes

Typical photos of the tight sandstone sample before and after the test are shown in Fig. 4. The alteration of porosity and permeability after salt precipitation obtained from our laboratory investigations are shown in Table 2 and Fig. 5. As shown in Table 2, the pore volume, porosity and permeability of the samples with different initial water saturation were reduced after salt precipitation, indicating that the porosity decrease by 1.62% ~ 14.53%, with an average of 8.27%, and the permeability can decrease by 10.04% ~ 64.70%, with an average of 32.83%.

Figure 5a presents the change in the porosity–permeability relationship of the specimens before and after salt precipitation. The figure demonstrates that most of the data points shift to the lower left, which indicates that salt precipitation causes a significant reduction in the porosity and permeability of the samples. The near linear relationship between porosity reduction (100%-$\phi_{\text{salt-precipitation}}/\phi \times 100$ %) and permeability reduction (100%-$k_{\text{salt-precipitation}}/k \times 100$%) is displayed in Fig. 5b. In particular, when the porosity reduction of the sample exceeds 7%, the permeability reduction is accelerated, a finding that is new and less than the critical porosity reduction given in a previous investigation

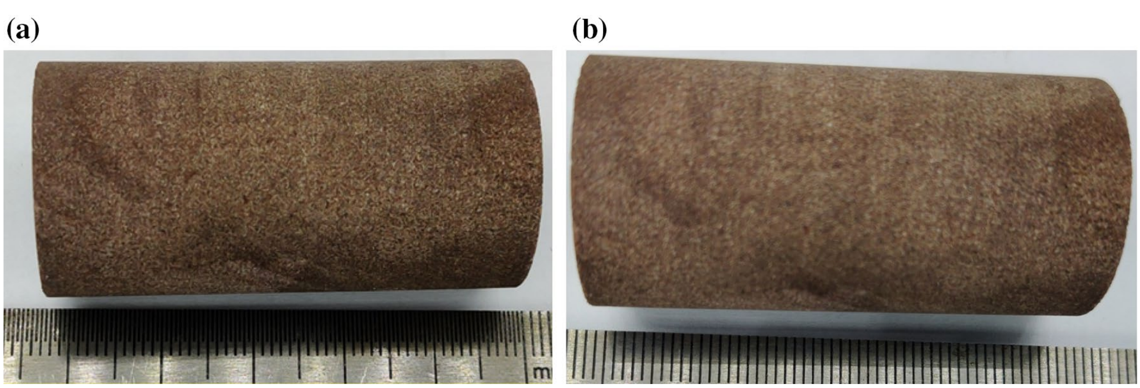

Fig. 4 Typical photos of a tight sandstone sample before and after the test. **a** Before salt precipitation; **b** after salt precipitation

Table 2 Porosity and permeability alteration of the samples after salt precipitation

Sample no.	Depth (m)	S_w (%)	$\phi_{salt\text{-}precipitation}$ (%)	$k_{salt\text{-}precipitation}$ ($\times 10^{-3}$ μm^2)	Porosity reduction (%)	Permeability reduction (%)	Pore volume after salt precipitation (cm^3)
KS5-4	7755.45	10	3.59	0.0211	3.28	12.41	0.817
KS5-5	7758.32	10	3.50	0.0206	1.62	10.04	0.368
KS3-4	7898.96	20	1.59	0.0249	5.79	18.30	0.314
KS3-9	7907.43	20	1.83	0.0175	5.13	15.91	0.412
KS4-1	7651.73	20	2.61	0.0110	6.62	13.79	0.617
KS6-7	7564.73	20	1.98	0.0115	6.86	15.12	0.484
KS5-12	7792.28	40	2.60	0.0110	7.21	35.84	0.461
KS5-14	7794.37	40	2.35	0.0109	9.07	39.95	0.269
KS5-13	7793.57	60	2.34	0.0076	12.11	52.94	0.371
KS5-15	7795.01	60	2.53	0.0066	13.69	53.19	0.373
KS1-17	7851.82	100	2.43	0.0049	13.38	61.71	0.285
KS1-23	7971.77	100	2.91	0.0116	14.53	64.74	0.376

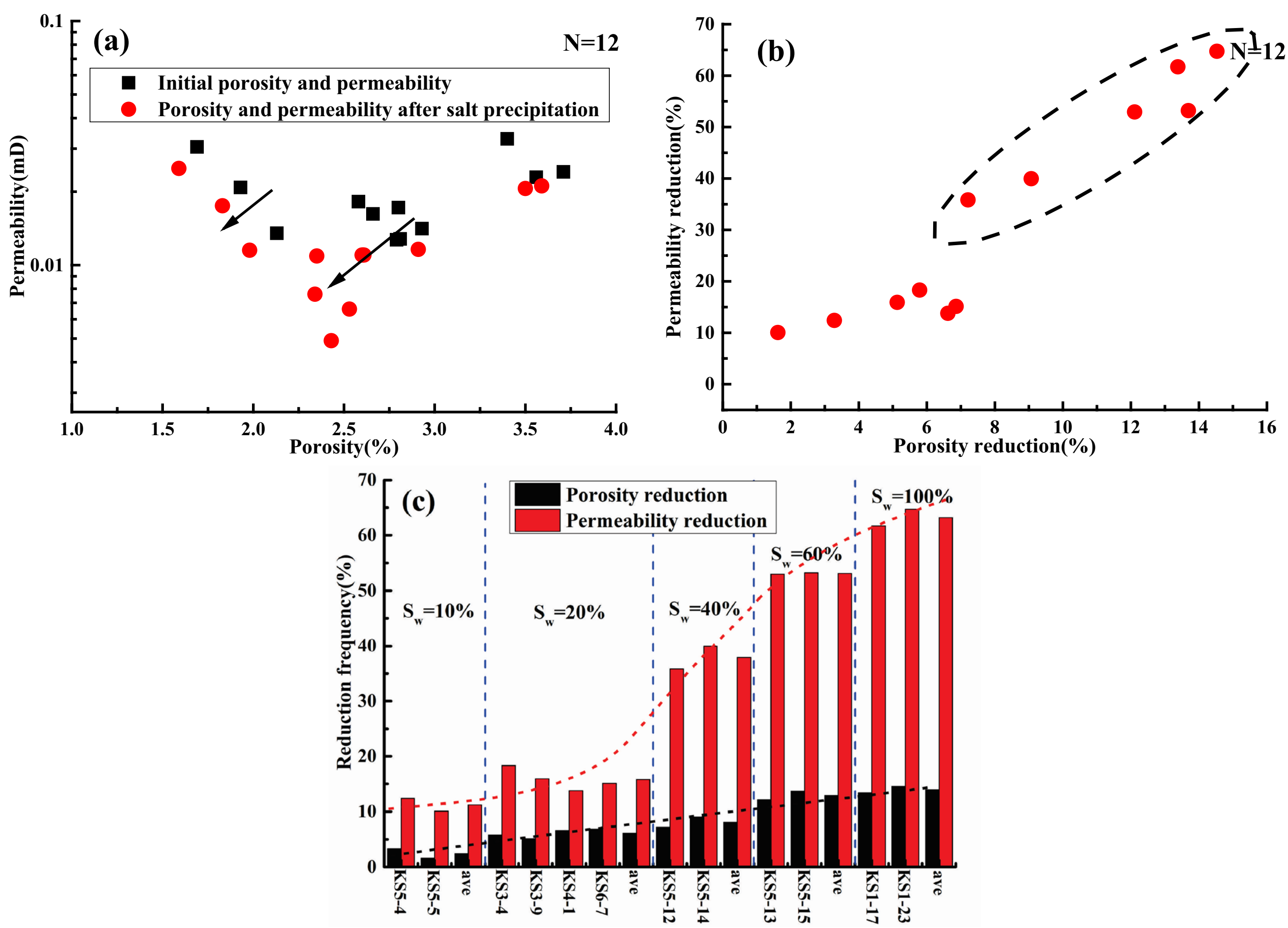

Fig. 5 **a** Porosity–permeability relationship before and after salt precipitation with different initial water saturation, **b** porosity reduction-permeability reduction relationship before and after salt precipitation with different initial water saturation, **c** the effect of water saturation on the porosity and permeability reduction after salt precipitation with different initial water saturation

(Tang et al. 2015). Preliminary analysis suggests that both the porosity and permeability of the samples used in this research are less than the values cited in the literature, and natural micro-fractures, as opposed to micro-fracture created by salt precipitation, play a more important role in gas seepage. Part of the porosity reduction followed salt precipitation is due to a reduction in the fracture space (fracture width). According to the cubic law (Witherspoon et al. 1980; Liu et al. 2000), small changes in the fracture space (fracture width) will induce large changes in fracture permeability. Therefore, the influence of the porosity reduction on the reduction of permeability is more noticeable in the tight sandstone samples tested. In addition, Fig. 5c shows the porosity and permeability reduction in samples at different water saturation levels after salt precipitation. When the water saturation levels in the samples were 10%, 20%, 40%, 60% and 100%, the average porosity reductions were 2.25%, 6.10%, 8.14%, 12.90% and 13.96%, respectively. At the same saturation levels, the average permeability reductions were 11.23%, 15.78%, 37.90%, 53.07% and 63.23%, respectively. It can be seen that as the initial water saturation increases, the reduction of porosity and permeability also increases. The reduction of permeability increases nonlinearly with the increase of water saturation, whereas the increase in the reduction of porosity is linear. The growth trend of the permeability reduction is more pronounced than that of the reduction of porosity.

3.2 Change of Permeability-Stress Sensitivity

The alterations to the porosity and permeability due to salt precipitation cause changes in the permeability stress sensitivity (Li et al. 2013). In general, porosity and permeability changes in the Precipitation Zone is large. Meanwhile, the variation of the effective stress in this region is also obvious during gas production. Figure 6 presents the representative evolution of permeability as a function of the effective stress during the loading and unloading pressurization phases for

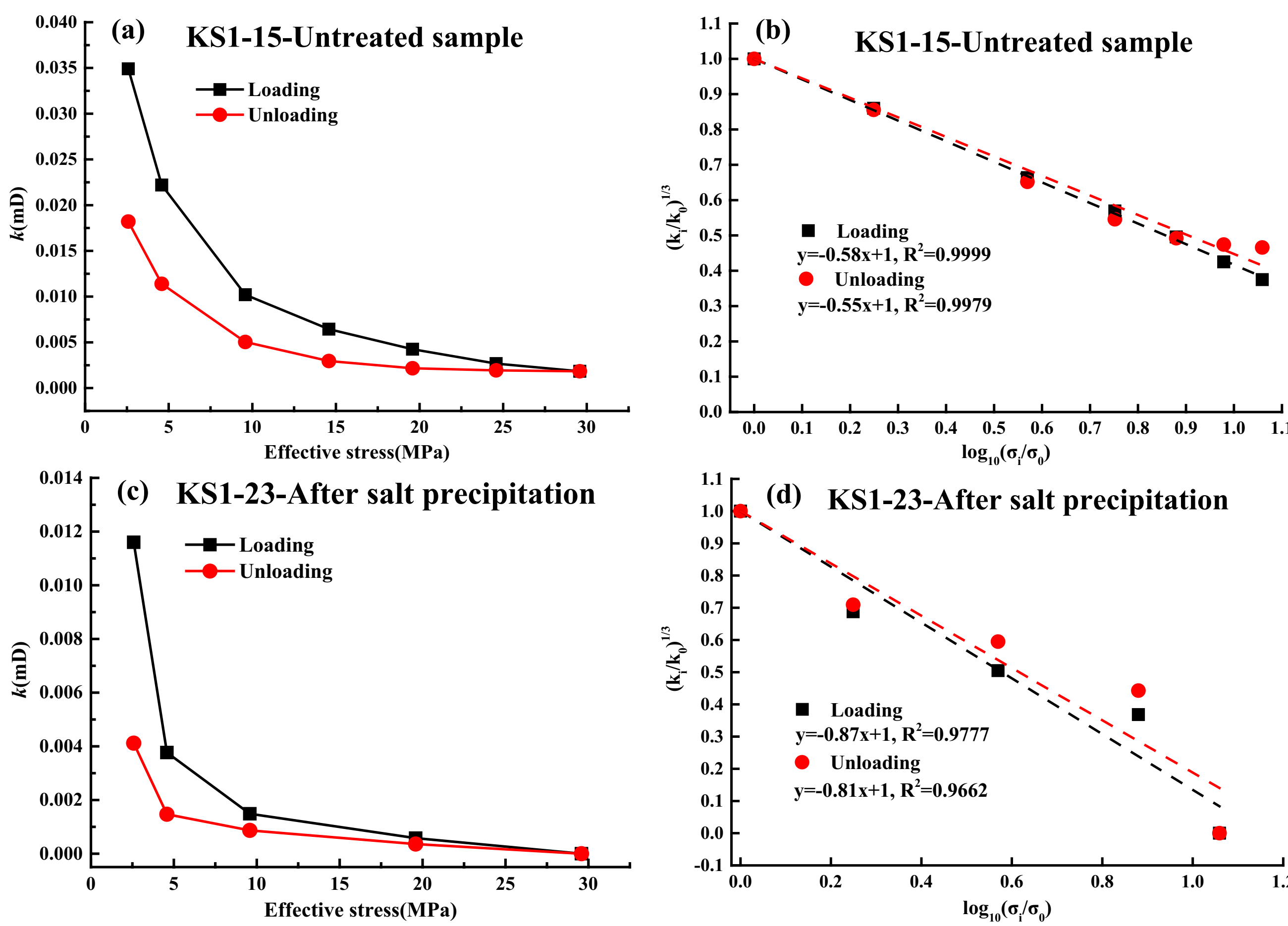

Fig. 6 The changes of permeability-stress sensitivity before and after salt precipitation. **a** Permeability evaluation of KS1-15 under different effective stresses, **b** the fitted result for the relationship between normalized permeability and normalized effective stress for KS1-15, **c** permeability evaluation of KS1-23 under different effective stresses, **d** the fitted result for the relationship between normalized permeability and normalized effective stress for KS1-23

an untreated tight sandstone sample (KS1-15) and a sample tested after salt precipitation (KS1-23). The irreducible permeability reduction with effective stress is similar to that observed by Selvadurai and Glowacki (2008) and Głowacki and Selvadurai (2016) for intact Indiana limestone and by Selvadurai (2015) for fractured granite. As we can see, the permeability reduction patterns for the sample after salt precipitation are similar to that of the untreated sample, but there is a pattern of deterioration compared to the untreated samples.

Table 3 presents a summary of the stress sensitivity coefficient changes of the samples before and after salt precipitation. Results indicate that the average stress sensitivity coefficients of the untreated specimens during the loading and unloading phases were 0.55 and 0.48, respectively. The average stress sensitivity coefficients of the samples after salt precipitation during the loading and unloading phases were 0.89 and 0.82, respectively. The results indicate that the degree of permeability-stress sensitivity damage of the tight sandstone is increased after salt precipitation. As consequence, the permeability-stress sensitivity changes could result in additional production losses during the same production time, and it is important to understand the mechanism of the permeability-stress sensitivity changes to control such losses. A preliminary analysis suggests that the permeability of the samples decreases after salt precipitation, and the size of the seepage channels in the rock are likely to be reduced, which leads to a permeability reduction under an almost identical deformation induced by confining pressure. A more detailed mechanism is discussed below based on the results of microstructural observations.

3.3 Variations of Elastic Wave Velocities

Figure 7a, b shows the variation in the elastic wave velocities of the tight sandstone samples before and after salt precipitation, and indicates that (1) the longitudinal wave velocity (V_p) decreases significantly after salt precipitation, and (2) the drop ranges from 5.01 to 14.66%, with an average of 10.12%. Similarly, the shear wave velocity (V_s) also decreases after salt precipitation, and the drop ranges from 8.70 to 23.02%, with an average of 15.91%. The drop range of the longitudinal wave velocity increased as the water saturation level increased; however, the downward trend in shear wave velocity was not obvious with changes in the water saturation level. Young's modulus (E) and Poisson's ratio (v) are important indictors related to the mechanical properties of rock (Davis and Selvadurai 1996; Villarraga et al. 2018), and usually they includes static data and dynamic data. Due to non-destructive property of the tests, the dynamic Young's modulus and the dynamic Poisson's ratio, i.e., Young's modulus and Poisson's ratio calculated by the elastic wave velocity, were select to characterize the changes in the rock mechanical properties after salt precipitation. The bulk density of the sample ρ (kg/m^3), V_p (km/s) and V_s (km/s) can be used to calculate E (MPa) and v, as follows (Jaeger et al. 2009):

$$E = \rho \frac{V_s^2\left(3V_p^2 - 4V_s^2\right)}{\left(V_p^2 - V_s^2\right)} \tag{3}$$

$$v = \frac{\left(V_p^2 - 2V_s^2\right)}{2\left(V_p^2 - V_s^2\right)} \tag{4}$$

The dynamic Young's modulus and the dynamic Poisson's ratio before and after salt precipitation were calculated based on the obtained ultrasonic data. In this research, the average density of the tight sandstone was 2550 kg/m^3. Figure 7c, d shows the evolution of E and v after salt precipitation for the samples at different initial water saturations (KS5-12 and KS5-14 with 40% water saturation; KS5-13 and KS5-15 with 60% water saturation; KS1-17 and KS1-23 with 100% water saturation). As shown in Fig. 7c, after salt precipitation the dynamic Young's modulus of the samples decreases significantly, with an average of a 14.60% reduction. The difference in E before and after salt precipitation increases significantly as the initial water saturation increases. The average reduction of E in the samples with 40%, 60% and 100% water saturation was 5.35%, 17.05%

Table 3 Permeability stress sensitivity experimental results before and after salt precipitation

Untreated samples				Samples after salt precipitation			
Sample no.	Depth (m)	Confining pressure condition	S_{si}	Sample no	Depth (m)	Confining pressure condition	S_{si}
KS1-7	7733.38	Loading	0.51	KS1-17	7851.82	Loading	0.90
		Unloading	0.42			Unloading	0.83
KS1-15	7850.46	Loading	0.58	KS1-23	7971.77	Loading	0.87
		Unloading	0.54			Unloading	0.81
Average	–	Loading	0.55	Average	–	Loading	0.89
		Unloading	0.48			Unloading	0.82

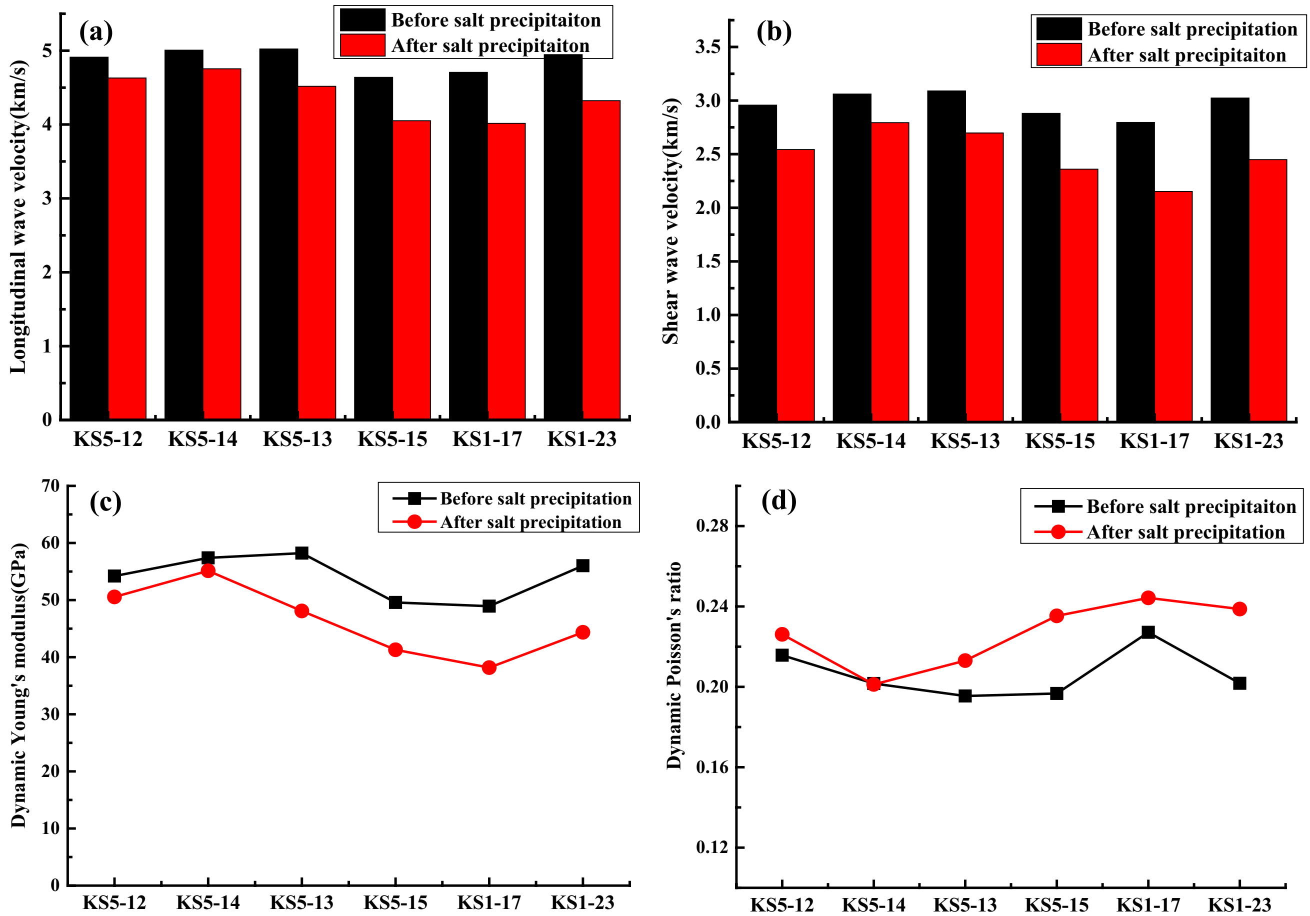

Fig. 7 **a** The change in the velocity of the longitudinal wave before and after salt precipitation, **b** the change in the velocity of the shear wave before and after salt precipitation, **c** the change in the dynamic Young's modulus before and after salt precipitation, **d** the change in the dynamic Poisson's ratio before and after salt precipitation

and 21.41%, respectively. As shown in Fig. 7d, the dynamic Poisson's ratio increases after salt precipitation, with an average increase of 9.85%. The dynamic Poisson's ratio increase in the samples with 40%, 60% and 100% water saturation is 2.29%, 14.31% and 12.94%, respectively, and it appears that the amount of precipitated crystalline salt has little influence on the changes in v.

3.4 Microstructural Analysis

3.4.1 Pore Distribution Analysis

The capillary pressures and pore characterization parameters of the tight sandstone before and after salt precipitation were measured using a high-pressure mercury injection test. Based on the assumption of cylindrical pores, the pore size distribution can be calculated by the Washburn equation (Yao and Liu. 2012): $R_c = (-2\sigma \cos \theta)/P_c$, where P_c is the absolute injection pressure, R_c is the pore radius (μm) when mercury enters at a pressure of P_c (MPa); θ is the contact angle between mercury and the pore surface; and σ is the interfacial tension of mercury. Therefore, it is not difficult to find that if the injection curve has a high slope and a very small flat section, only a small proportion of the pores have the same diameter; the higher the slope and the smaller flat section, the smaller the proportion of the pores with the same diameter, i.e., intense heterogeneity of the pore-throat size. Figure 8 shows the representative curves for mercury intrusion and evacuation of the samples. There is only a very small flat section in the mercury injection curves before and after salt precipitation, which indicates that the pore-throat size is predominantly heterogeneous. Meanwhile, the curves shift to the top right after salt precipitation, which indicates that, to achieve the same mercury saturation, the injection pressure has to be higher. Furthermore, the slope of the curve is smaller after salt precipitation, indicating that the heterogeneity of the pore throat becomes greater after salt precipitation. As shown in Table 4, the average threshold pressure of the samples before and after salt precipitation was 1.31 MPa and 1.21 MPa, respectively. The average

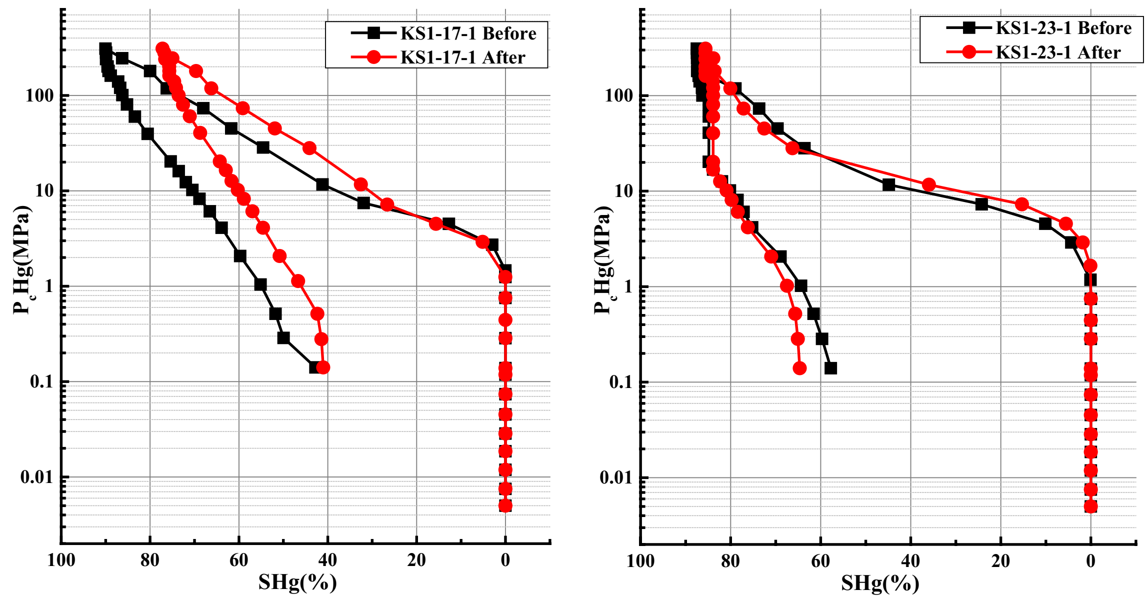

Fig. 8 The mercury intrusion and evacuation curves of tight sandstone before and after salt precipitation

Table 4 Parameters of pore throat structure of the samples before and after salt precipitation by high-pressure mercury injection test

Cores	Threshold pressure (MPa)	Median saturation pressure (MPa)	Average pore throat Radius (μm)	Uniformity coefficients	Sorting coefficient	Efficiency of mercury withdrawal (%)
KS1-17-1 before	1.43	22.83	0.0322	0.1844	2.3420	52.49
KS1-17-1 after	0.75	40.94	0.0180	0.3088	3.3591	46.87
KS1-23-1 before	1.18	16.24	0.0452	0.1877	2.2618	34.00
KS1-23-1 after	1.66	19.34	0.0380	0.1925	2.2895	24.45

median saturation pressure before and after salt precipitation was 19.54 MPa and 30.14 MPa, respectively. Also, the corresponding median pore-throat radius is 0.0387 μm and 0.0280 μm. The average efficiency of mercury withdrawal before and after salt precipitation is 43.25% and 35.66%, respectively. The low mercury recovery efficiency indicates that the samples consisted of a system of large body pores interconnected by very narrow pore throats (Lai et al. 2018), and the dimension ratio of these pore throats become larger after salt precipitation as evidenced by the lower average efficiency of mercury withdrawal. On the whole, the average pore throat radius decreases significantly, and the pore throat geometries become more complex after salt precipitation.

Figure 9 presents the corresponding permeability contribution ratio due to different pore radii in tight sandstone before and after salt precipitation. The curves of the permeability contribution ratio shift to the lower left after salt precipitation, and the maximum permeability contribution ratio decreases significantly. In other words, the effect of the bigger pores on the seepage of rock samples is reduced, and the permeability contribution of the bigger pore throat becomes smaller. On the other hand, a great number of the small pores become the main seepage channel after salt precipitation. It is likely that the larger pores and pore throats are separated into smaller ones because of salt precipitation, so that eventually, the smaller pores and pore-throats become the main seepage channels. As a corollary, the permeability of the samples would decrease dramatically after salt precipitation (Yun et al. 2009), which was observed in the experimental results of permeability alteration shown in Fig. 5c in Sect. 3.1.

3.4.2 Image Analysis of Crystalline Salt

Both type and crystallization position of the crystalline salt are vital when examining the impact of salt precipitation on the physical, mechanical and transport properties of the tight sandstone. Results of Energy Dispersive X-Ray Spectroscopy (EDX) analysis after salt precipitation are shown in Fig. 10a, where a mass of crystalline salt

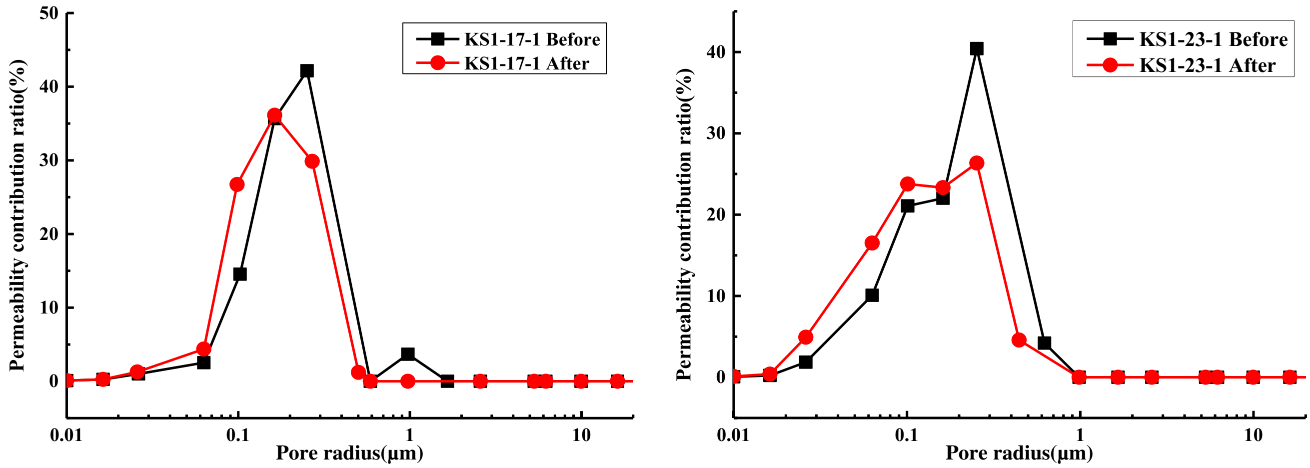

Fig. 9 Permeability contribution ratio by different pore radius of tight sandstone before and after salt precipitation

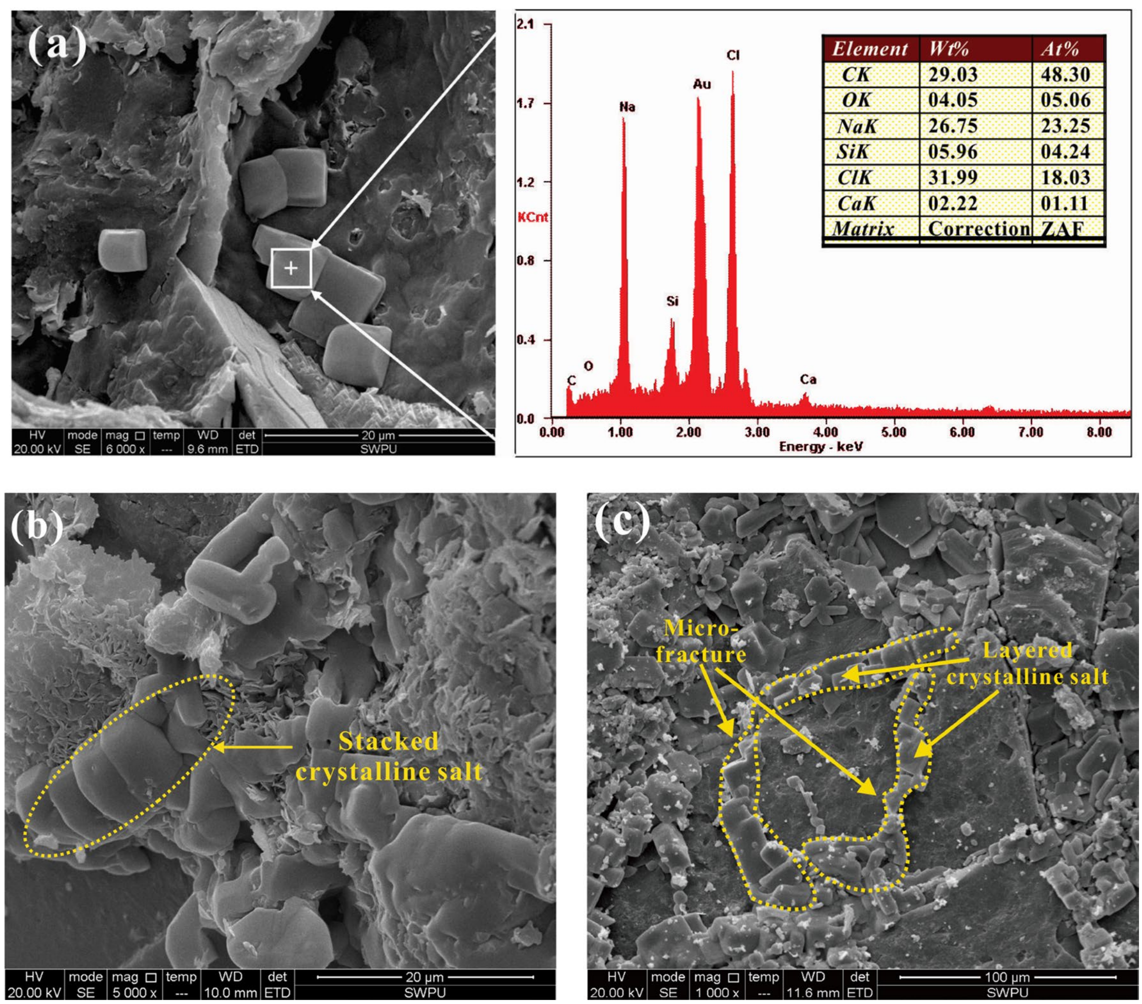

Fig. 10 **a** SEM images and EDX analyses on the crystalline salt, **b** the stacked crystalline salt developed on the surface of Illite/smectite inter-stratified mineral, **c** micro-fracture that was plugged with the layered crystalline salt

is clearly seen on the fracture surface of the samples. As determined by the EDX analysis, carbon, nitrogen, oxygen, sodium, chlorine and calcium were present in the crystalline salt, with high percentages of both sodium and chlorine. Therefore, after taking into account the composition of the brine solution as shown in Table 1, the preliminary analysis suggests that the main type of salt that crystallized in the samples was sodium chloride. Furthermore, Fig. 10b shows that crystalline salt stacks that developed on the surface of clay minerals (an illite/smectite interstratified mineral in this figure) are widely distributed. Clay minerals are mainly observed in the pore throats and fractures, and therefore, the stacked crystalline salt reduces both the porosity and permeability of the material. These results explain the porosity and permeability reduction of the tight sandstone after salt precipitation.

In addition, Steiger (2005) indicates that the crystallization pressure induced by inorganic salt is negatively correlated with the molar volume of inorganic salts. Due to its smaller molar volume than common double salt, the crystallization pressure induced by NaCl is the largest. Therefore, it is easy to conclude that sodium chloride can cause deformation and damage to sandstone due to drying-induced salt crystallization pressure. Figure 10c shows micro-fracture that was obstructed by the layered crystalline salt. Based on the theory of fracture mechanics, the stress intensity factor induced by the crystalline salt located in the tip of the fracture easily exceeds the critical stress intensity factor of the fracture, causing secondary cracks (Coussy 2006), and this possibility has been demonstrated by Ju (2014).

3.5 Physico-Chemical Coupling Mechanism Analysis

To obtain a more accurate analysis, the fracture tip strength factor induced by salt precipitation was modeled Zhang et al. (2019). The simplified mechanical model is shown in Fig. 11.

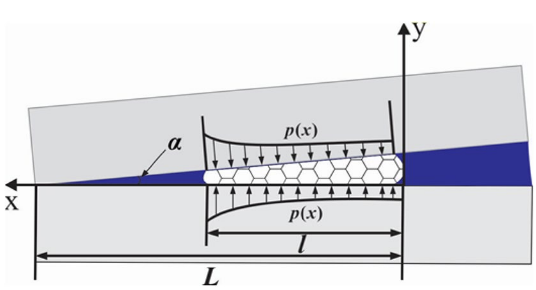

Fig. 11 The distribution of crystallization stress in the wedge fracture (Ju 2014)

The formula for calculating the stress intensity factor is as follows:

$$K_{\mathrm{I}} = \frac{\gamma_{\mathrm{CL}}}{\tan(\alpha/2)\sqrt{\pi L}} \int_0^l \frac{1}{L-l}\left(\frac{L+l}{L-l}\right)^{1/2} dl, \qquad ((5))$$

where γ_{CL} is interfacial free energy of sodium chloride, J/m^2; L is the distance between the tip of fracture and the location of salt precipitation, m; l is the length of the crystalline salt, m, α is the fracture opening angle, °; K_{I} is the stress intensity factor, MPa m$^{1/2}$. For a fracture of 1 m long or shorter, K_{I} induced by salt precipitation easily exceeded the fracture toughness of tight sandstone. In other words, micro-fracture in the tight sandstone sample will propagate under the action of salt precipitation, which will increase the amount of damage in the tight sandstone sample. Consequently, the mechanical properties of the samples decrease. The experimental results given in Sect. 3.3 show that the impact of salt precipitation on the dynamic Young's modulus and dynamic Poisson's ratio was significant, which is in agreement with the SEM image analysis results. Meanwhile, due to the reduction of the Young's modulus and Poisson's ratio, the specimens tested after salt precipitation were more prone to deformation (Głowacki and Selvadurai 2016; Zhu et al. 2018).

4 Conclusion

Representative samples from ultra-deep tight sandstone gas reservoirs with high-salinity brine obtained from the Tarim Basin, were used in the research to investigate changes to the physical and mechanical properties caused by salt precipitation resulting from the evaporation of the formation water. The main finding of this research can be summarized as follows:

Both porosity and permeability of the tight sandstone decrease significantly after salt precipitation (Porosity reduction of 1.62% ~ 14.53%, with an average of 8.27%; permeability reduction of 10.04% ~ 64.70%, with an average of 32.83%). When the reduction in the porosity of the sample exceeds 7%, the permeability reduction is noticeable. The higher the initial water saturation, the larger the range of the porosity and permeability loss. The degree of permeability-stress sensitivity damage in the tight sandstone was increased after salt precipitation. The average stress sensitivity coefficients of the samples after salt precipitation during the loading and unloading phases were 0.89 and 0.82, respectively, while the average stress sensitivity coefficients of the untreated samples during the loading and unloading phases were 0.55 and 0.48, respectively.

The elastic wave velocities of the tight sandstone decreased significantly after salt precipitation. The ultrasonic spectrum analysis suggested that the dynamic Young's modulus of the rock decreased by 14.60% on average, and the dynamic Poisson's ratio increased by 9.85% on average, which indicates that salt precipitation has a tendency to weaken the rock matrix.

The microstructural analysis suggests that the main type of salt crystallized is sodium chloride; the smaller pores and throats become the main seepage channel after salt precipitation, because the crystalline salt is mainly deposited on the surface of any particles and in the pores and natural microfractures. Salt precipitation and subsequent occlusion of the pore spaces not only reduces the porosity and permeability, but also creates secondary cracks, leading to a weakened rock matrix. The changes in the seepage channels and rock mechanical strength can help to explain the deterioration of the permeability-stress sensitivity after salt precipitation.

Acknowledgements This work was funded by the National Science Foundation of China (Nos. 51604236, 51674209), the Sichuan Province Youth Science and Technology Team Project (No. 2016TD0016) and the China Scholarship Council (CSC No. 201708510127). The authors would like to thank Mrs. Sally Selvadurai, Assist-Ed Editorial Service, Montréal, Canada for her editing of the manuscript.

Compliance with Ethical Standards

Conflict of Interest The authors declare that they have no conflict of interest.

References

Biot MA (1941) General theory of three-dimensional consolidation. J Appl Phys 12:155–164

Borgia A, Pruess K, Kneafsey TJ, Oldenburg CM, Pan L (2012) Numerical simulation of salt precipitation in the fractures of a CO_2-enhanced geothermal system. Geothermics 44:13–22

Coussy O (2006) Deformation and stress from in-pore drying-induced crystallization of salt. J Mech Phys Solids 54(8):1517–1547

Cui GD, Ren SR, Zhang L, Ren B, Zhuang Y, Li X, Han B, Zhang PF (2016) Formation water evaporation induced salt precipitation and its effect on gas production in high temperature natural gas reservoirs. Petrol Explor Dev 43(5):815–824

Cui GD, Ren SR, Rui ZH, Ezekiel J, Zhang L, Wang H (2018) The influence of complicated fluid-rock interactions on the geothermal exploitation in the CO_2 plume geothermal system. Appl Energy 227:49–63

Davis RO, Selvadurai APS (1996) Elasticity and geomechanics. Cambridge University Press, Melbourne

Dehghanpour H, Lan Q, Saeed Y, Fei H, Qi Z (2013) Spontaneous imbibition of brine and oil in gas shales: effect of water adsorption and resulting microfractures. Energy Fuels 27(6):3039–3049

Espinosa-Marzal RM, Scherer GW (2010) Advances in understanding damage by salt crystallization. Acc Chem Res 43(6):897–905

Espinosa-Marzal RM, Scherer GW (2013) Impact of in-pore salt crystallization on transport properties. Environ Earth Sci 69(8):2657–2669

Flatt RJ (2002) Salt damage in porous materials: how high supersaturations are generated. J Cryst Growth 242:435–454

Flatt RJ, Caruso F, Sanchez AM, Scherer GW (2014) Chemo-mechanics of salt damage in stone. Nat Commun 5:4823

Głowacki A, Selvadurai APS (2016) Stress-induced permeability changes in Indiana limestone. Eng Geol 215:122–130. https://doi.org/10.1016/j.enggeo.2016.10.015

Jaeger JC, Cook NG, Zimmerman R (2009) Fundamentals of rock mechanics, 4th edn. Wiley, Hoboken

Ju XD (2014) Study on the mechanism of crystallization damage for the porous media of rocks. Doctoral dissertation, Retrieved form Wanfang database **(in Chinese)**

Kim KY, Han WS, Oh J, Kim T, Kim JC (2012) Characteristics of salt-precipitation and the associated pressure build-up during CO_2 storage in saline aquifers. Transport Porous Med 92:397–418

Kirk JW, Dobbs JB (2002) A protocol to inhibit the formation of natrium chloride salt blocks. In: International Symposium on Oilfield Scale, 30–31 January, Aberdeen

Kleinitz W, Koehler M, Dietzsch G (2001) The precipitation of salt in gas producing wells. In: SPE European formation damage conference, 21–22 May, The Hague

Lai J, Wang GW, Cao JT, Xiao CW, Wang S, Pang XJ, Dai QQ, He ZB, Fan XQ, Yang L, Qin ZQ (2018) Investigation of pore structure and petrophysical property in tight sandstones. Mar Petrol Geol 91:179–189

Le D, Mahadevan J (2011) Productivity loss in gas wells caused by salt deposition. SPE J 16:908–920

Li S, Tang DZ, Pan ZJ, Xu H, Huang WQ (2013) Characterization of the stress sensitivity of pores for different rank coals by nuclear magnetic resonance. Fuel 111:746–754

Liu J, Elsworth D, Brady BH, Muhlhaus HB (2000) Strain-dependent fluid flow defined through rock mass classification schemes. Rock Mech Rock Eng 33(2):75–92

Miri R, Hellevang H (2016) Salt precipitation during CO_2 storage—a review. Int J Greenh Gas Con 51:136–147

Noiriel C, Renard F, Doan ML, Gratier JP (2010) Intense fracturing and fracture sealing induced by mineral growth in porous rocks. Chem Geol 269:197–209

Ott H, Andrew M, Snippe J, Blunt MJ (2014) Microscale solute transport and precipitation in complex rock during drying. Geophys Res Lett 41(23):8369–8376

Rathnaweera TD, Ranjith PG, Perera MSA (2015) Effect of salinity on effective CO_2 permeability in reservoir rock determined by pressure transient methods: an experimental study on Hawkesbury sandstone. Rock Mech Rock Eng 48(5):2093–2110

Rijniers L, Huinink H, Pel L, Kopinga K (2005) Experimental evidence of crystallization pressure inside porous media. Phys Rev Lett 94:075503

Scanlon BR, Tyler SW, Wierenga PJ (1997) Hydrologic issues in arid, unsaturated systems and implications for contaminant transport. Rev Geophy 35:461–490

Selvadurai APS (2015) Normal stress-induced permeability hysteresis of a fracture in a granite cylinder. Geofluids 15:37–47. https://doi.org/10.1111/gfl.12107

Selvadurai APS (2018) The Biot coefficient for a low permeability heterogeneous limestone. Contin Mech Therm 31(4):939–953

Selvadurai APS, Głowacki A (2008) Permeability hysterisis of limestone during isotropic compression. Groundwater 46(1):113–119. https://doi.org/10.1111/j.1745-6584.2007.00390.x

Selvadurai APS, Zhang DJ, Kang YL (2018) Permeability evolution in natural fractures and their potential influence on loss of productivity in ultra-deep gas reservoirs of the Tarim Basin, China. J Nat Gas Sci Eng 58:162–177

Shahidzadeh-Bonn N, Desarnaud J, Bertrand F, Chateau X, Bonn D (2010) Damage in porous media due to salt crystallization. Phys Rev E 81:066110

Steiger M (2005) Crystal growth in porous materials-I: the crystallization pressure of large crystals. J Cryst Growth 282:455–469
Tang Y, Yang RZ, Du ZM, Zeng FH (2015) Experimental study of formation damage caused by complete water vaporization and salt precipitation in sandstone reservoirs. Transp Porous Med 107(1):205–218
Tian J, You LJ, Luo PY, Kang YL, Zhang DJ (2018) Experimental investigation on liquid permeability of tight rocks under back pressure conditions. J Petrol Sci Eng 169:421–427
Van Dorp QT, Slijkhuis M, Zitha PLJ (2009) Salt precipitation in gas reservoirs. In: SPE European Formation Damage Conference, 27–29 May, Scheveningen
Villarraga C, Gasc-Barbier M, Vaunat J, Darrozes J (2018) The effect of thermal cycles on limestone mechanical degradation. Int J Rock Mech Min 109:115–123
Winkler EM, Singer PC (1972) Crystallization pressure of salts in stone and concrete. Geol Soc Am Bull 83(11):3509–3514
Witherspoon PA, Wang JSY, Iwai K, Gale JE (1980) Validity of cubic law for fluid flow in a deformable rock fracture. Water Resour Res 16(6):1016–1024
Xu CY, Lin C, Kang YL, You LJ (2018) An experimental study on porosity and permeability stress-sensitive behavior of sandstone under hydrostatic compression: characteristics, mechanisms and controlling factors. Rock Mech Rock Eng 51:2321–2338
Yao YB, Liu DM (2012) Comparison of low-field NMR and mercury intrusion porosimetry in characterizing pore size distributions of coals. Fuel 95:152–158
Yun MJ, Yu BM, Cai JC (2009) Analysis of seepage characters in fractal porous media. Int J Heat Mass Tran 52:3272–3278
Zhang DJ, Kang YL, You LJ, Li JX (2018) Investigation of formation damage induced during drill-in process of ultra-deep fractured tight sandstone gas reservoirs. J Energy Resour-ASME Online. https://doi.org/10.1115/1.4042236
Zhang DJ, Kang YL, You LJ, Li XC (2019) Rock strength degradation induced by salt precipitation: a new mechanical mechanism of sand production in ultra-deep fractured tight sandstone gas reservoirs. In: 53rd US Rock Mechanics/Geomechanics Symposium, 23–26 June, New York City, New York
Zheng H, Feng XT, Jiang Q (2015) The influence of NaCl crystallization on the long-term mechanical behavior of sandstone. Rock Mech Rock Eng 48(1):33–51
Zhou H, Hu D, Zhang F, Shao J, Feng X (2016) Laboratory investigations of the hydro-mechanical–chemical coupling behaviour of sandstone in CO_2 storage in aquifers. Rock Mech Rock Eng 49(2):417–426
Zhu SY, Du ZM, Li CL, You ZJ, Peng XL, Deng P (2018) An analytical model for pore volume compressibility of reservoir rock. Fuel 232:543–549
Zhuang Y, Liu XJ, Xiong HQ, Liang LX (2018) Microscopic mechanism of clay minerals on reservoir damage during steam injection in unconsolidated sandstone. Energy Fuel 32(4):4671–4681